Cardiovascular Engineering and Technology, Vol. 3, No. 4, December 2012 *(© 2012)* pp. 450–461
DOI: 10.1007/s13239-012-0112-8

Fluid Mechanics of Mixing in the Vertebrobasilar System: Comparison of Simulation and MRI

MATTHEW D. BOCKMAN,[1] AKASH P. KANSAGRA,[2] SHAWN C. SHADDEN,[3] ERIC C. WONG,[4,5] and ALISON L. MARSDEN[1]

[1]Department of Mechanical and Aerospace Engineering, University of California, San Diego, CA, USA; [2]Department of Radiology and Biomedical Imaging, University of California, San Francisco, CA, USA; [3]Department of Mechanical, Materials, and Aerospace Engineering, Illinois Institute of Technology, Chicago, IL, USA; [4]Department of Radiology, University of California, San Diego, CA, USA; and [5]Department of Psychiatry, University of California, San Diego, CA, USA

(Received 30 May 2012; accepted 22 October 2012; published online 7 November 2012)

Abstract—Recent magnetic resonance imaging (MRI) studies have demonstrated that perfusion to the posterior fossa of the brain can be surprisingly unilateral, with specific vascular territories supplied largely by a single vertebral artery (VA) rather than a mixture of the two. It has been hyposthesized that this is due to a lack of mixing in the confluence of the VA into the basilar artery (BA), however the local mechanisms of mixing (or lack thereof) have not been previously examined in detail. This study aims to assess the mixing characteristics and hemodynamics of the vertebrobasilar junction using subject specific computational fluid dynamics (CFD) simulations, and perform quantitative comparisons to arterial spin labeling (ASL) MRI measurements. Subject specific CFD simulations and unsteady particle tracking were performed to quantitatively evaluate vertebrobasilar mixing in four subjects. Phase-contrast MRI was used to assign inflow boundary conditions. A direct comparison of the fractional flow contributions from the VAs was performed against perfusion maps generated *via* vessel-encoded pseudo-continuous arterial spin labeling (VEPCASL) MRI. The laterality of VA blood supply in 7/8 simulated cerebellar hemispheres and 5/7 simulated cerebral hemispheres agree with ASL data. Whole brain laterality of the VA supply agrees within 5% for measured and computed values for all patients. However, agreement is not as strong when comparing perfusion to individual regions. Simulations were able to accurately predict laterality of VA blood supply in four regions of interest and confirm ASL results, showing that very little mixing occurs at the vertebrobasilar confluence. Additional particle tracking analysis using Lagrangian coherent structures is used to augment these findings and provides further physical insight that complements current *in vivo* imaging techniques. A quantitative mix-norm measure was used to compare results, and sensitivity analysis was performed to assess changes in the results with pertubations in the boundary condition values.

Address correspondence to Alison L. Marsden, Department of Mechanical and Aerospace Engineering, University of California, San Diego, CA, USA. Electronic mail: mdbockma@ucsd.edu, amarsden@ucsd.edu

Keywords—Computational fluid dynamics, Arterial spin labeling, MRI, Lagrangian coherent structures, Fluid mixing, Vertebral artery, Basilar artery.

INTRODUCTION

The vertebrobasilar system includes the left and right vertebral arteries (VAs) as well as their confluence into the basilar artery (BA). As the only arterial confluence of this size in the human body, the vertebrobasilar junction exhibits unique fluid mixing characteristics, providing an opportunity to compare simulation and imaging methods aimed at mapping flow patterns and quantifying mixing. This may provide a basis for the intelligent design of targeted drug delivery techniques and other endovascular interventions in future work.

Recent advances in patient specific modeling for cardiovascular flow have included anatomic model construction with increasing level of detail, physiologic lumped parameter boundary conditions, fluid structure interaction, and automated surgery optimization.[10,29,32,50] These tools have been applied to improve understanding of hemodynamics and disease processes in pediatric cardiology, coronary artery disease, cerebral aneurysms, and many other applications.[2,21,27,28,30,31,36] While there has been an abundance of work characterizing flow in the carotid arteries and in cerebral aneurysms both *in vitro* and in simulations,[3,6,43] there have been relatively few studies examining the hemodynamics of the vertebrobasilar junction. Vertebral artery (VA) flow in an idealized geometry was studied experimentally *in vitro* by Lutz,[26] who found little mixing of VA flow in the BA. Krijger

studied flow patterns in the BA confluence using finite element simulations in a symmetric, rectangular cross section, 3D idealized geometry with rigid walls and steady flow,[20] and concluded that 3D models are necessary to accurately characterize vertebrobasilar flow, which differed greatly from previous 2D models.[19]

Arterial spin labeling (ASL), developed in 1992 by Williams *et al.*,[11,48] is an magnetic resonance imaging (MRI) method that uses water in arterial blood as a freely diffusible tracer of perfusion. This method was originally used to image global brain perfusion, but recent vessel-encoded pseudo-continuous ASL (VEPCASL) methods have been employed to map perfusion from specific arteries.[9,12,14,15,46,47,49,52,53] VEPCASL allows spin labeling in a single 2D plane, enabling the study of perfusion of long and tortuous arteries. Results from a recent VEPCASL study performed by Kansagra and Wong showed that VA perfusion territories in the cerebellum are relatively distinct, suggesting minimal mixing of flow from the two VAs within the BA.[17] Their results suggest that there is minimal mixing of flow from the right and left VAs in the BA. Because the ASL is not natively capable of examining local hemodynamics, the use of computational fluid dynamics (CFD) provides a complementary method for comparison, and sheds further light on the flow physics of the vertebrobasilar system.

Subject specific CFD modeling can provide detailed hemodynamic information, such as wall shear stress and 3D mixing patterns, that is not readily available through most standard imaging modalities *in vivo*. Although CFD simulations have been validated against *in vitro* data in several studies,[22,23] fewer results on direct validation with *in vivo* data exist.[1,4] While not a full validation, this study provides a much needed direct, quantitative comparison of simulation predictions with *in vivo* data in multiple human subjects, as well as a novel use of Lagrangian particle tracking data. Quantification of particle tracking is important for studying blood perfusion, which has applications for targeted drug delivery and improving flow distribution, for example to prevent arteriovenous malformations in congenital heart disease patients.[33,51]

It is difficult, and often impossible, to visually track fluid advection from the transient 3D fluid velocity fields and streamlines that are produced from CFD simulations. Lagrangian particle tracking[25,39] can be used to integrate mass-less tracer particles in fluid velocity fields and quantify fluid advection. Additionally, Lagrangian coherent structures (LCS), a recently developed method for distinguishing structures in unsteady flow, can be used to visualize and understand mechanisms of fluid transport.

Additional mixing quantification is performed in this study with an advection-diffusion solver, allowing for a direct measure of the degree of mixing. Both the LCS and advection-diffusion methods provide important and complementary insight into the mixing characteristics in the VAs. Post processing of the convection-diffusion simulation results enables a single measure for mixing to be used for quantification *via* variance and mix-variance calculations.

The primary purpose of this study is to investigate the mixing characteristics of the vertebrobasilar junction. The secondary purpose of this study is to compare VEPCASL findings and CFD simulations by assessing the mixing characteristics of the vertebrobasilar junction in multiple subjects, thereby providing an opportunity for cross-comparison of ASL and CFD data. The rest of the paper is organized as follows. We first discussion model construction and simulation methods. We then make comparisons of brain perfusion, including ASL methods, with simulation. We then analyze mixing hemodynamics and Lagrangian measures. Finally, we present conclusions and discussion.

MODEL CONSTRUCTION AND SIMULATION METHODS

Four healthy volunteers (age 23–24, 1 male, 3 females, see Table 1) without known cerebrovascular disease were included in this study after providing informed consent. The local Institutional Review Board approved the study protocol, which was conducted in accordance with institutional guidelines.

3D patient specific models were constructed from subjects magnetic resonance angiography (MRA) data using a custom version of the open source SimVascular package (simtk.org).[38] The VAs, anterior

TABLE 1. Demographic information.

	Age	Sex	Anatomy	Left VA inflow ($cm^3 \cdot s^{-1}$)	Right VA inflow ($cm^3 \cdot s^{-1}$)
Subject 1	31	F	Normal	2.09	1.43
Subject 2	25	M	Normal	0.82	0.46
Subject 3	23	F	Normal	0.99	0.95
Subject 4	24	F	Right fetal P1	1.90	1.43

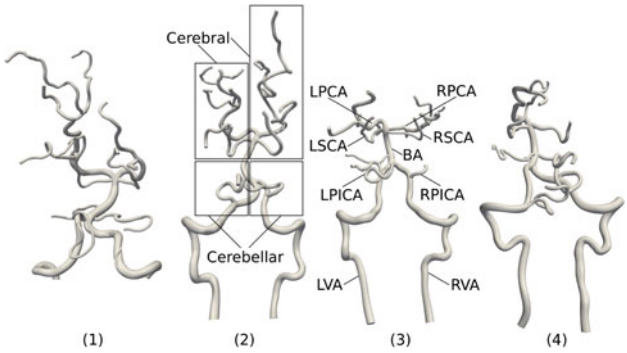

FIGURE 1. 3D patient specific models based on MRA data. PCA = posterior cerebral artery, SCA = superior cerebellar artery, BA = basilar artery, AICA = anterior inferior cerebellar artery, VA = vertebral artery.

inferior cerebellar arteries (AICAs), superior cerebellar arteries (SCAs), posterior cerebral arteries (PCAs), posterior inferior cerebellar arteries (PICAs) and posterior communicating arteries were modeled, where patient-specific anatomy allowed, in addition to smaller resolvable branches (Fig. 1). This resulted in two inlets at the VAs, 4–7 outlets in the cerebellar region, and 8–12 outlets in cerebral region. As illustrated in Fig. 2, the 3D model building process started with overlaying 3D volumetric MRA data with paths along each modeled artery. Along these paths, segmentations were drawn manually along the blood-vessel lumen, followed by lofting segmentations together to form the fluid domain. Multiple arterial branches were merged to form the vertebrobasilar vasculature. At each intersection, blending was done to eliminate artificially discontinuous junctions. A tetrahedral mesh was created for each model, and adapted to ensure mesh convergence over four iterations using MeshSim (Simmetrix Inc.), with the final meshes containing approximately 750,000 elements.

At the left and right VA inlet faces of the model a time-varying inflow boundary condition was prescribed. Because only time-averaged phase-contrast MRI data was collected, a characteristic VA waveform from the literature was scaled, for the left and right VAs, to the mean values for each subject to create the transient inflow boundary conditions.[13] The waveform spanned one cardiac cycle (Fig. 3).

Resistance boundary conditions were applied to the outlets,[44] with values assigned to be inversely proportional to the outlet areas, and constrained such that the sum of all parallel resistances equals total hydraulic resistance R, satisfying $P = QR$, where P is the blood pressure and Q is the volumetric flow rate. For our simulations, the mean arterial pressure was assumed to be 115 mmHg, and the volumetric flow rate was the sum of the mean flowrates of the VAs.

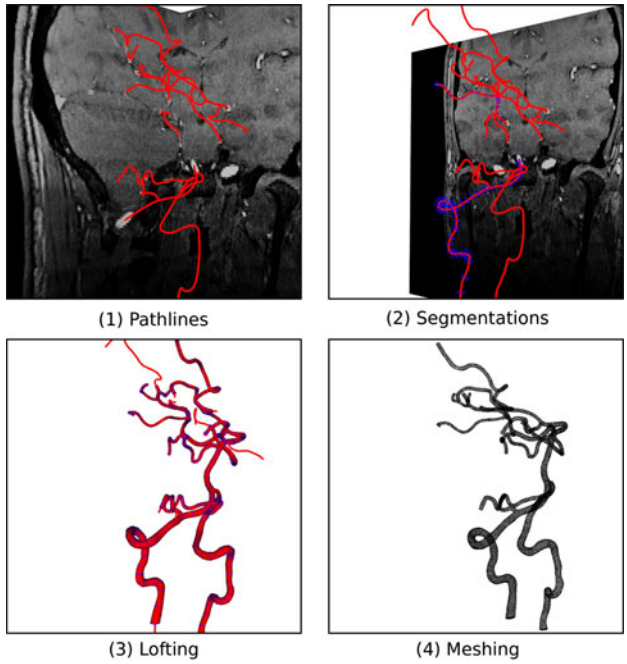

FIGURE 2. Model creation process from MRA data.

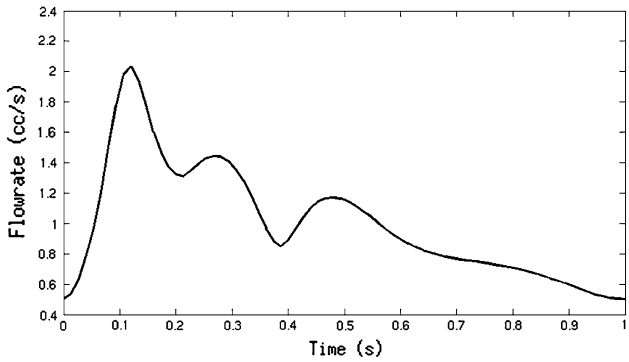

FIGURE 3. Normalized VA inflow waveform.

Hemodynamic simulations were performed by solving the time-dependent 3D Navier–Stokes equations assuming a viscous, Newtonian, incompressible fluid with a rigid wall approximation. A custom finite element flow solver was employed, using a generalized α-method time integration scheme with 2nd order numerics.[16] Viscosity and density of blood were assigned the values of $\mu = 0.04$ g^{1}cm^1 s^{-1} and $\rho = 1.06$ g^{1}cm^{-3}, respectively. The average Reynolds number was approximately 200 with a peak of 400. The Schmidt number was 377,000. Time varying inflow conditions were defined for one cardiac cycle with a period of 1 s, and repeated over the course of 6 simulated cardiac cycles. Each cycle was simulated using 1000 time steps, with a time step size of 1 ms. The velocity fields from the last cardiac cycle was used for

post processing (Fig. 4). Simulations were performed on a CentOS 5.2 linux-based cluster using 4–48 CPU cores (AMD Opteron 2378, 2.4 ghz Quad-Core) and required approximately 45 CPU hours.

QUANTIFICATION OF BRAIN PERFUSION

MRI Methods

Each of the four patients was scanned using a Signa Excite 3.0T short bore MR scanner (General Electric Medical Systems, Milwaukee, WI) with a commercial 8-channel head coil. For locating anatomical features, a 3D time-of-flight, spoiled gradient echo MRA was performed with a resolution of 0.4 mm × 0.4 mm × 1.0 mm, TR/TE 20/2.7 ms, and 15° flip angle on 32 separate slices in each of 3 slabs. An axial labeling plane was then chosen approximately 50 mm below the circle of Willis. Twelve imaging slices were positioned parallel to and roughly 30 mm above the labeling plane for VEPCASL and anatomical T1 imaging. VEPCASL scans were performed with a resolution of 2.2 × 2.2 × 5.0 mm, TR/TE 3300/3.0 ms, and 40 excitations in each of two interleaves using single shot spiral acquisition with fat saturation (Fig. 5). Additional parameters were as described in Kansagra and Wong.[17] Performance of two VEPCASL scans allowed for differentiation of internal carotid artery (ICA) perfusion from VA perfusion, and left and right territories, respectively. A single axial phase contrast MR image at the level of the labeling plane allowed measurement of volumetric flow rates of the ICAs and VAs; this image was obtained at 0.4 mm × 0.4 mm × 4.0 mm resolution with TR/TE 50/12 ms and 30° flip angle. The literature reports a coefficient of variation (noise-to-signal ratio) of 9.0% for non-triggered sequences (non-triggered was used in our study), with an average difference between measured flow and real flow of 8.3%, in a phantom model.[42,45]

MATLAB (MathWorks, Natick, MA) was used to generate VA perfusion territory maps. A posterior perfusion fraction mask was computed from the ratio of VA to total perfusion in each voxel (Fig. 5, Row 2). The left-right perfusion image was multiplied with the posterior perfusion fraction mask on a voxelwise basis to suppress ICA contribution to left-right structure, leaving only the left-right structure of VA perfusion. Using anatomical T1 slices taken at the same location as VEPCASL slices, four regions of interest (ROIs) comprising the left and right cerebral and cerebellar hemispheres were manually defined. For each ROI, the VA supply fraction was quantified as the cumulative VA perfusion to total perfusion within that ROI (Fig. 5, Row 4). The error of the supply fraction is estimated to be 11%.[18] The reproducibility of ASL is reported to be approximately 3.5%.[7]

Phase-contrast MRI data was first processed using MATLAB by subtracting a baseline (known zero velocity) from the image. Each VA was isolated from the image (cropping), and all voxels below a threshhold velocity of 1 cm^1s^{-1} were discarded to isolate the VA from surrounding tissue. The velocity was integrated over this region to obtain the time-averaged volumetric flow rate of each VA. The values found correlate to published values.[52,53]

Particle Tracking Simulation Methods

Using the simulated velocity fields, mass-less tracer particles were advected through the fluid domain using a customized Lagrangian particle tracking code (Fig. 6).[39,41] For this study, it was assumed that mixing due to diffusion was negligible due to the large ratio of advection to diffusion and that particles did not interact with each other.

Approximately 1000 uniformly spaced tracer particles were seeded at each VA inlet for each 1/50th of one cardiac cycle. Final tracer positions were computed by

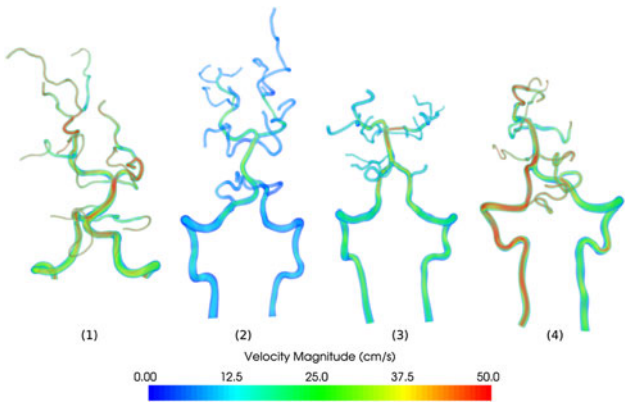

FIGURE 4. Volume rendering of velocity magnitude of all four subjects near systole.

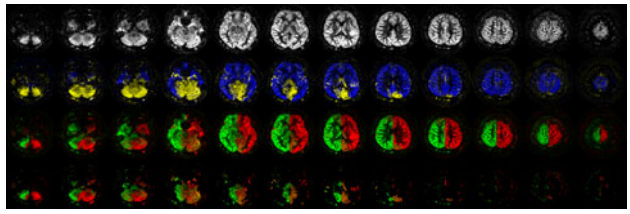

FIGURE 5. Vessel-encoded pseudo-continuous ASL perfusion maps. *Row 1*: Total perfusion. *Row 2*: Perfusion of ICAs (blue) and VAs (yellow). *Row 3*: Perfusion of right ICA/VA (green) and left ICA/VA (red). *Row 4*: right (green) and left (red) VA perfusion.

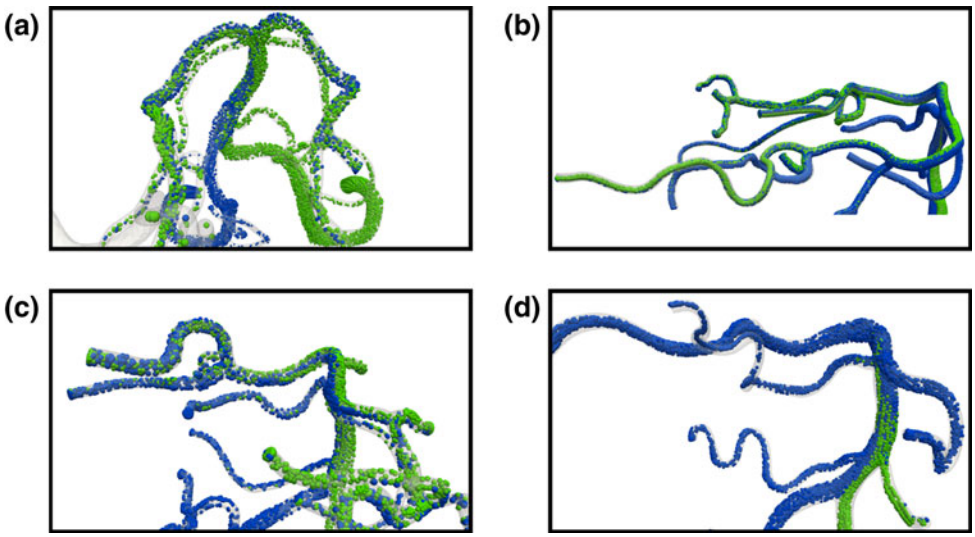

FIGURE 6. Results of vertebrobasilar flow simulation demonstrating relatively little VA mixing in the BAs or PCAs of (a) subject 1, (b) subject 2, (c) subject 3, (d) subject 4.

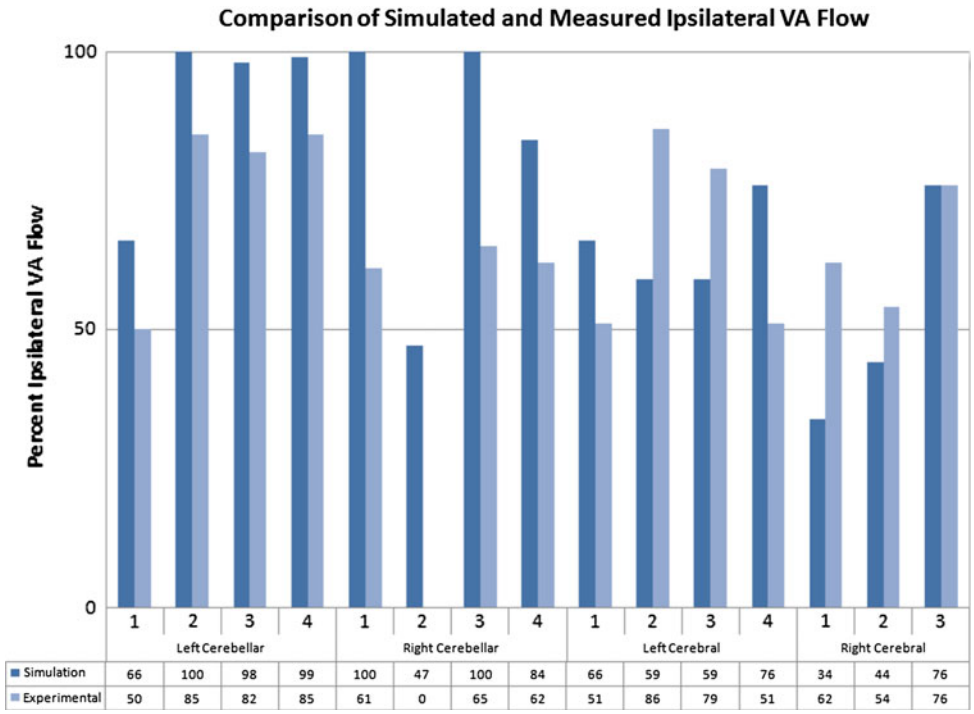

FIGURE 7. Percentage of ipsilateral flow for each subject over the four regions of interest for both simulated and experimental results.

numerically integrating the CFD-derived velocity data using a Runge-Kutta-Fehlberg scheme and linear interpolation. Particles were integrated for ten cardiac cycles to ensure that most seeded tracers reached the outlets; a small minority of tracers that did not reach the outlets due to near-zero velocity near walls were discarded. Particle quantity and flux were summed at each of outlet and mapped to the four ROIs. Tracers were weighted by initial flux to accurately use each particle as a representation of a discrete volume of fluid.

Each outlet of the model was assigned to one of the four defined ROIs based on its location. The flux weighted quantities of all particles for all outlets of a particular region were summed to compute the total contribution of a particular VA to that region.

Particle Tracking Perfusion Results and Comparison to MRI

The laterality of VA perfusion as measured by ASL and computed by simulation for each subject is summarized in Table 2, listing left and right VA contributions to the cerebellum and cerebrum hemispheres. A bar chart of the ipsilateral flow contribution to each region is shown in Fig. 7.

In the left and right cerebellar hemispheres, simulations revealed 7/8 hemispheres were perfused predominantly by the ipsilateral VA while 53% of the flow to the remaining hemisphere was supplied by the contralateral VA supply. Of all 8 cerebellar hemispheres, an average of 87 ± 19% of the flow was supplied by the ipsilateral VA. Experimentally, 6/8 cerebellar hemispheres were perfused predominantly by the ipsilateral VA, 1/8 hemispheres was supplied equally by both VAs, and the remaining hemisphere was completely perfused by the contralateral VA. Additionally, the experimental results show that 61 ± 28% cerebellar hemisphere perfusion flow was supplied by the ipsilateral VA.

Because of the variant anatomy of subject 4, who had a diminutive right PCA owing to fetal configuration, only 7 cerebral hemispheres could be evaluated using simulation. Of the 7 cerebral hemispheres considered, 5 (71%) were primarily supplied by the ipsilateral VA (matching experimental data in 5/5 cases). 1/7 had slight contralateral dominance (56% contralateral perfusion, subject 2, right cerebrum), which matched well with the experimental data (46% contralateral perfusion) despite reverse laterality. 66% of the flow to the remaining cerebral hemisphere (subject 1, right cerebrum) was supplied by the contralateral VA, which did not match the laterality of experimental data (experimentally, only 38% of the flow to this hemisphere was from the contralateral VA).

In addition to quantifying VA supply to the cerebellar and cerebral hemispheres, laterality of the VA supply to the SCAs, AICAs, and PICAs was characterized. In the subjects with appropriate vasculature, 62 ± 32% of the flow was supplied to the SCAs (the furthest cerebellar artery downstream of the VA-BA confluence) by the ipsilateral VA. Both the AICAs and PICAs had virtually complete ipsilateral VA supply, with 99.5 ± 0.6% and 100 ± 0% ipsilateral supply, respectively. While dominant ipsilateral supply to the SCAs may not be intuitive, the dominant ipsilateral supply to the AICAs makes sense due to their location just downstream of the VA-BA confluence. The PICAs are located on the VAs upstream the VA-BA confluence, so it naturally follows that they are completely supplied by the ipsilateral VA. Table 3 summarizes the ipsilateral VA contributions to the brain.

Whole brain perfusion is calculated as the ratio of unilateral VA supply to overall VA supply. This data is calculated based on the time-averaged flow rate assigned to the VAs as an inflow boundary condition. The value used for the numerical simulations was derived from the PCMRI data, as described in Fig. 5. An average of 58 ± 5% of perfusion to the whole brain was supplied from the dominant VA in simulation, compared to 57 ± 7% in experiment, showing little dominance of the VAs. All subjects had primarily left VA perfusion to the whole brain, matching experimental data.

VA perfusion to the cerebellar hemispheres are highly ipsilateral in most subjects, as shown in Fig. 8. VA perfusion to the cerebrum is less markedly ipsilateral than to the cerebellum, but mixing of flow streams from the right and left VAs is minimal, as shown in Fig. 8. At the confluence of the VAs, left and right VA contributions remain relatively unmixed. Some mixing starts occurring approximately 70% of the BA length downstream of the confluence.

Sensitivity Analysis

To determine the sensitivity of results to changes in the outflow boundary conditions, the resistance of a large outlet in the right cerebral region of subject 1 was

TABLE 2. Simulation and experimental vertebral artery contributions to cerebellum and cerebrum.

		Cerebellum				Cerebrum				Whole brain	
	VA supply	L, Sim (%)	L, Exp (%)	R, Sim (%)	R, Exp (%)	L, Sim (%)	L, Exp (%)	R, Sim (%)	R, Exp (%)	Sim (%)	Exp (%)
Subject 1	Left	66	50	0	39	66	51	66	38	59	52
	Right	34	50	100	61	34	49	34	62	41	48
Subject 2	Left	100	85	53	100	59	86	56	46	64	67
	Right	0	15	47	0	41	14	44	54	36	33
Subject 3	Left	98	82	0	35	59	79	23	34	51	56
	Right	2	18	100	65	40	21	77	76	49	44
Subject 4	Left	99	85	16	38	76	51	N/A	31	57	53
	Right	1	15	84	62	24	49	N/A	69	43	47

TABLE 3. Ipsilateral VA contributions, computed from particle tracking, to the left/right superior cerebellar, anterior inferior cerebellar, and posterior inferiror cerebellar arteries.

	LSCA (%)	RSCA (%)	LAICA (%)	RAICA (%)	LPICA (%)	RPICA (%)
Subject 1	54	95	100	100	100	N/A
Subject 2	100	3	N/A	N/A	100	100
Subject 3	80	37	99	99	100	100
Subject 4	51	74	99	100	100	100

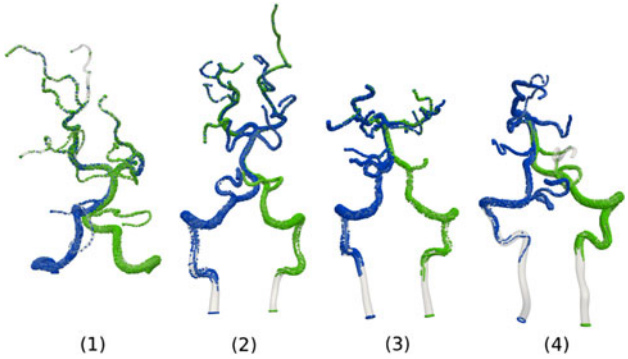

FIGURE 8. Particle advection through the vertebrobasilar system. Blue particles seeded at left VA, green seeded at right VA.

varied ±10%, and other resistances were adjusted accordingly to satisfy conservation of mass. These two variations were then simulated using the same procedures used in the nominal cases.

The ipsilateral flow to each region in subject 1 was within 1.2% of nominal value for both cases. These results indicate that results were not sensitive to changes in a single outflow boundary condition relative to the others.

HEMODYNAMICS OF THE BASILAR ARTERY

While the MRI findings provide overall perfusion numbers to different regions of the brain, they cannot readily provide insight into local hemodynamics or mixing mechanisms. To provide a mechanistic explanation for the observed lack of mixing, we use two approaches. First, LCS are computed from the particle advection simulations. This provides a method for visualizing unsteady flow fields and provides a physical understanding. Second, we further quantify the mixing using a convection diffusion solver, to extract a single mixing measure, using either a variance or mix-norm. Qualitative observation reveals that VA blood remains unmixed in the BA for approximately 2/3 to 3/4 of the length of the BA. Mixing downstream is relatively minor, as shown in the right SCA of subject 3 (Fig. 6). In subjects 1 and 2 there is an apparent helical flow through the BA to the SCAs.

LCS

Using the particle advection fields, LCS were computed using Finite-time Lyapunov exponents (FTLE) to illustrate the mixing characteristics in the flow field, using methods described in Shadden *et al.*[40] The FTLE was computed over an integration step of 0.1 seconds with a resolution of 300 particles per centimeter (27 million particles per cubic centimeter). At the confluence of the VAs, the FTLE was computed with reverse time (giving insight into converging particles), whereas at the bifurcation forward time was used (giving insight into diverging particles).

The FTLE is defined as

$$\sigma(\mathbf{x},t,\tau)=\frac{1}{2|\tau|}ln\lambda_{\max}(\mathbf{S}(\mathbf{x},t,\tau)) \tag{1}$$

where

$$\mathbf{S}(\mathbf{x},t,\tau)=\left(\frac{d\phi_t^{t+\tau}(\mathbf{x}(t))}{d\mathbf{x}(t)}\right)^T\left(\frac{d\phi_t^{t+\tau}(\mathbf{x}(t))}{d\mathbf{x}(t)}\right) \tag{2}$$

is a finite-time version of the right Cauchy–Green deformation tensor and $\lambda_{\max}(\mathbf{S}(\mathbf{x},t,\tau))$ denotes the maximum eigenvalue of the linear operator $\mathbf{S}(\mathbf{x},t,\tau)$.[39] τ is the time interval which the velocity field is integrated to get the flow map $\phi_t^{t+\tau}:\mathbf{x}(t)\mapsto\mathbf{x}(t+\tau)$.

Figure 9 shows the Finite-time Lyapunov exponents computed for subject 1. The red FTLE "ridge" defines an LCS, which is a material boundary separating flow with distinct origin (backward time FTLE) or distinct destination (forward time FTLE). In the forward-time computations of the bifurcation, areas of greater magnitude (red) illustrate greater separation between neighboring particles, which e.g. indicates the boundary between flow streams to the left and right PCAs. In the reverse-time FTLE, areas of greater magnitude illustrate greater convergence (or divergence in backward time), which e.g. indicates the boundary between flow streams from the left and right VAs. The plots show distinct fluid regions, in both the converging and diverging sections, which qualitatively confirms the lack of mixing. These results demonstrate lack of mixing local to the confluence and bifurcation of the BA. The LCS clearly shows regions of the flow which are destined for particular vessel branches. The third

slice from the top in Fig. 9 shows a green region in the center of the BA. The second slice from the top shows that region being elongated, and the top slice shows that region branching off to the subject's right PCA.

Convection Diffusion and Mix-Variance

While LCS can provide mechanistic insight, and indeed confirms the lack of mixing observed in MRI, it is difficult to reduce these results to a single quantitative measure of mixing. For this purpose, we solve an additional convection diffusion equation as a post-processing step using the simulation results. The convection-diffusion equation models the convection and diffusion of a scalar in a velocity field. In this study, a tracing scalar was used to trace blood from the left and right VAs. The convection-diffusion equation is

$$\frac{\partial \phi}{\partial t} = \kappa \bigtriangledown^2 \phi - \mathbf{v} \cdot \bigtriangledown \phi \tag{3}$$

where ϕ is a scalar quantity of interest, κ is the diffusion coefficient, and $\mathbf{v}$ is the convection velocity vector derived from simulation. This equation was solved on the same mesh as the hemodynamic simulations using an in-house code. The convection-diffusion code uses a Streamline Upwind/Petrov-Galerkin formulation with a generalized α-method time integration scheme.[5] A diffusion coefficient of $\kappa = 10^{-7}$ cm^2 s^{-1} was used.[8] The convection velocity was was equal to the fluid velocity from the Navier–Stokes simulations. Dirichlet boundary conditions of $\phi = 1$ and $\phi = 0$ were assigned uniformly at the left and right vertebral inlets. The scalar, ϕ, was allowed to diffuse for 5 cardiac cycles, with uniform 1 ms timesteps.

Slices of the concentration field perpendicular to the path originally used to create the BA were created using an automated Paraview (Kitware, Inc, Clifton Park, NY) script with a uniform spacing of 0.25 mm. The unstructured 2D slice data was transformed to a regular grid. Of the points on the regular grid where valid data existed (inside the confines of the vessel lumen), both variance and mix-variance were computed and plotted as a function of distance along the BA. The variance is defined as:

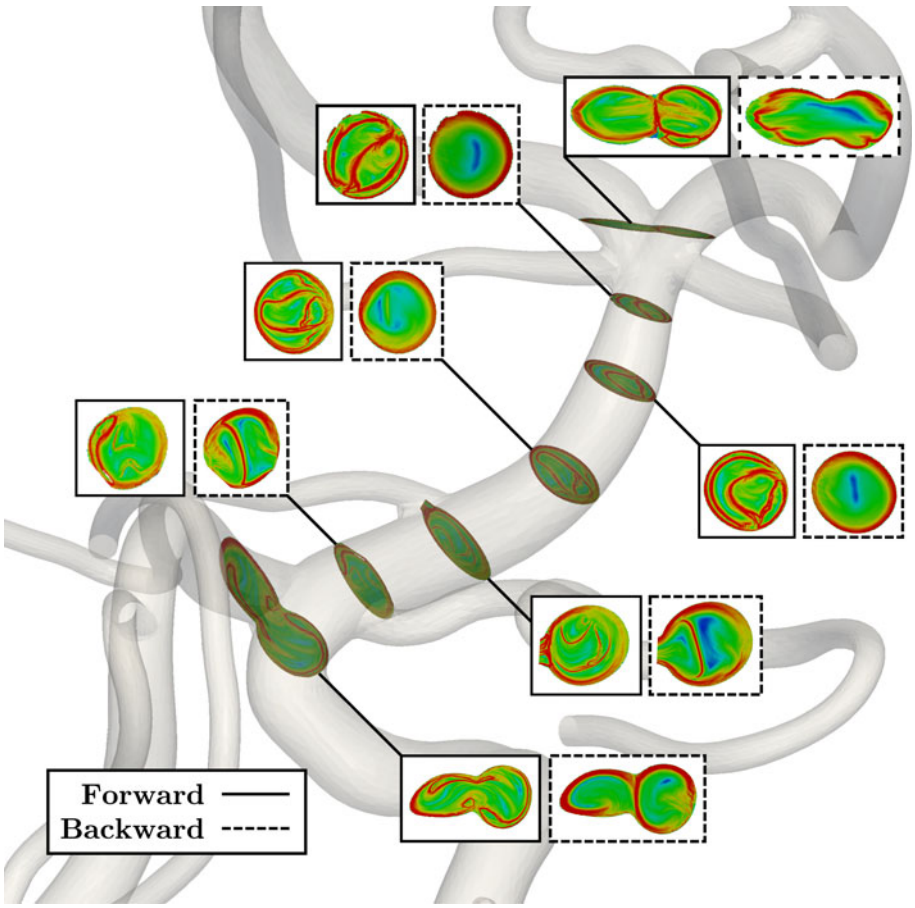

FIGURE 9. Slices of the forward and backward Finite-time Lyapunov exponents (FTLE) of subject 1.

$$\sigma^2 = \frac{1}{N}\sum_{i=1}^{N}(c_i - \overline{c})^2 \quad (4)$$

where N is the number of valid samples, c_i is the scalar value of the ith sample, and $\overline{c}$ is the mean of the scalar field. In the case of variance, the scalar field domain was mapped to a 2D rectilinear grid, and the nodes of the grid were sampled. The variance is defined as the square of the standard deviation and is proposed as a measure of mixing in Mathew *et al.*[34] However, in Mathew *et al.*,[34] one of the stated limitations mentioned is that the mixing can only be measured where sufficient particles accumulate. We address this concern using the continuous scalar field instead of using particle tracking. In the context of our study, a field containing an equal unmixed portion of both red-tagged ($c = 1$) and blue-tagged ($c = 0$) fluid represents a variance of 0.25, which we have normalized from zero to one. The mix-variance, defined in Mathew *et al.*,[35] builds on the standard variance by averaging the standard variance computed over different mesh sizes. Mix-variance accounts for mixing over a range of spatial scales, whereas standard variance only considers mixing on a single scale. Mix variance was computed for subject 1 and compared to standard variance (Fig. 10), with little difference.

Measures of mixing for all subjects are shown in Fig. 11 as a function of distance along the BA from the confluence to the bifurcation. Since variance and mix-variance gave similar results, variance was used as the mixing measure for all subjects. The normalized variance decreased from a quantity of 1 (unmixed) to a quantity of less than 0.1 (more mixed). There is a roughly linear relationship between location along the BA and the variance.

DISCUSSION

This study explores the mechanisms of mixing in the basilar artery using unsteady, subject-specific flow simulations, and provides a direct and quantitative comparison between novel MR perfusion imaging methods and subject specific CFD modeling. Local hemodynamics and mixing were quantified using LCS and a convection diffusion model to compute measures of mixing.

Simulation results confirmed an overall lack of mixing of the blood supplies from the two vertebral arteries into the BA, as well as in the cerebellar and cerebral hemispheres. Simulation predictions of cerebellar mixing agree well with experimental data in a global sense. The prediction of laterality of the dominant VA supplying each hemisphere was consistent with the experimental data. However, the actual average amount of flow provided to all cerebellar hemispheres by the ipsilateral VA did not agree well with experimental findings (87 ± 19% vs. 61 ± 28%). In addition, close agreement was found between experimental whole brain data, with VEPCASL findings, and the simulation whole brain data, based on phase-contrast MRI (PCMRI), which suggest that the PCMRI data and our method of extracting the volumetric flow rate is consistent with the VEPCASL data. In all cases, laterality in simulation and experimental data were well matched, with the exception that the left cerebellar hemisphere of Subject 1 did not have any dominant VA perfusion in the experimental data.

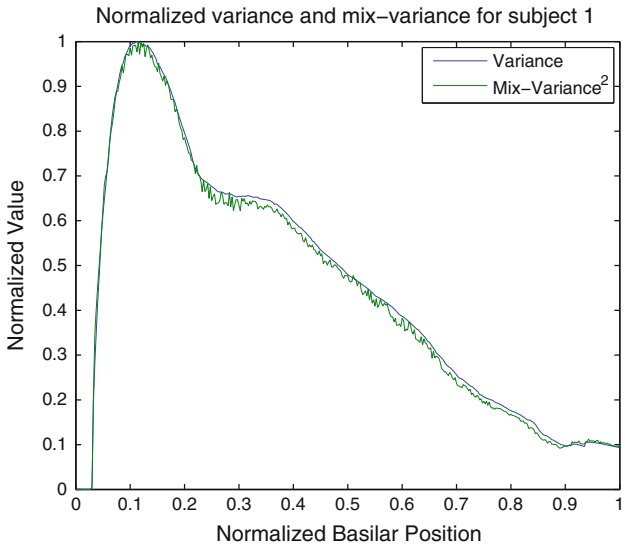

FIGURE 10. Comparison of variance and mix-variance squared for subject 1.

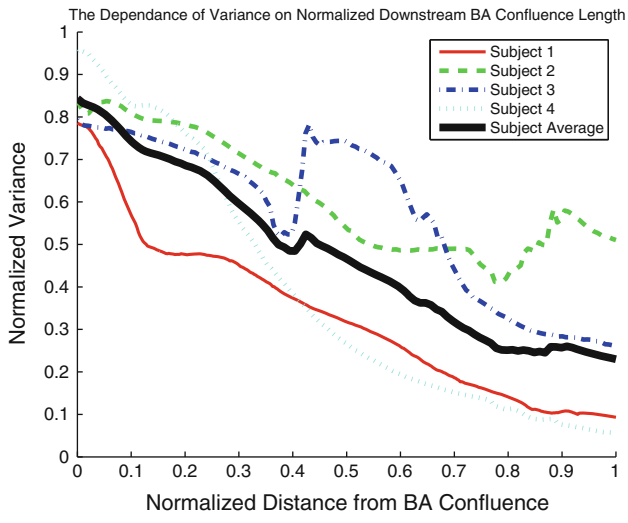

FIGURE 11. Time-averaged normalized variance as a function of BA location.

CFD results identify the presence of two weakly mixed streams of flow that persist for most of the length of the BA. This study confirms a surprising prior finding that there is relatively little mixing in the BA, and that this persists to certain regions of the brain. Quantification of VA perfusion to the cerebral ROIs shows somewhat more mixing than in the cerebellar ROIs. As this unmixed portion of the BA is the site of origin of most of the cerebellar arteries, this CFD finding lends credence to the hypothesized physical mechanism for the lack of mixing proposed in previous ASL MRI studies. Because the previous MRI studies did not examine local hemodynamics in the basilar artery, the prior work could only speculate that there were two distinct streams of fluid in the basilar artery, with little mixing. The simulations presented here fill this gap, at least qualitatively, and confirm the previous hypothesis.

The LCS results from subject 1 (Fig. 9) reveal the bilateral flow structures from the left and right vertebral arteries. They also show the distinct flow structures that result from the bifurcation and surrounding arteries at the end of the basilar artery.

By utilizing particle tracking to determine particle perfusion, advection paths can be visualized to different outlets of the model. By visualizing particles in this manner, potential targeted drug delivery injection sites could be identified. For example if one wanted to inject a drug targeted to the right cerebellar region, these findings would indicate that it should be injected in the right VA. Arteries or regions of interest can be mapped to areas where drug injection may be possible, and appropriate concentrations could be computed. This should be an area of future work.

While global mixing and laterality agreed very well, there were discrepancies in comparisons at the level of individual vessels. Discrepancies between experiment and simulation may result from differences in ROI definition, which is the main limitation of this study. ROIs used in VEPCASL analysis are easily defined based on anatomical T1-weighted MR images. Similar analysis in the CFD domain requires unique assignment of individual arterial outlets to corresponding anatomical ROIs, though it is possible these assignments are imperfect due the limited resolution of the MRA data. It is likely that due to vessel branching beyond the limits of MRA resolution, a single outlet may actually supply more than one ROI. This may explain why most data points have very close agreement, while a few data points in individual vessels deviate significantly from experimental values.

Additional limitations of this study are uncertainties in the inflow and outflow boundary conditions, and the use of a rigid wall approximation. While the lack of time-varying phase-contrast MRI data for inlet boundary conditions has been addressed by using a literature-derived VA waveform, this data is not patient specific. Outlet resistance boundary conditions are based on the outlet areas, which could be subject to variability. Furthermore, the use of RCR (Resistance–Capacitance–Resistance, or Windkessel) boundary conditions may be more physiological than the resistance conditions used here, as they allow for better prediction of the pressure waveform.[44] The sensitivity study provided additional confidence in the robustness of simulation results to small changes in boundary condition values. However, a full uncertainty quantification should be performed in future work following the methods presented in our recent work,[37] and this analysis should incorporate the uncertainties in the MRI measurements. The use of rigid walls has been shown to overestimate wall shear stress compared to the non-rigid case,[24] however, wall shear stress is not a parameter of interest in this study. The same study showed little difference in flow distribution between rigid and non-rigid cases, which supports the use of rigid walls in the present study.

The primary purpose of the study was to increase understanding of the mixing (or lack thereof) in the BA. The secondary purpose of this study was to perform a quantitative comparison between VEPCASL and CFD. Overall, our results confirm the prior hypothesis that little mixing occurred in the BA. Agreement between CFD and MRI was mixed, showing promise for the continued use of CFD to explain physical phemonemon and match global values, but room for improvement in making detailed predictions in individual vessels. We maintain that detailed hemodynamic information, such as LCS and mix-variance, may be obtained from CFD simulations that is difficult or impossible to obtain experimentally or in standard clinical imaging. Additionally, hypothetical scenarios could be evaluated in future work, such as targeted drug delivery or the effects of cerebrovascular disease on blood mixing.

ACKNOWLEDGMENTS

Support for this work was provided by a Burroughs Wellcome Fund Career Award at the Scientific Interface, a UCSD Collaboratories Grant and NIH grant R01EB002096. The authors gratefully acknowledge the use of software from the Simvascular open source project (simtk.org), and the convection-diffusion code written by Mahdi Esmaily Moghadam.

REFERENCES

[1]Arzani, A., P. Dyverfeldt, T. Ebbers, and S. C. Shadden. In vivo validation of numerical prediction for turbulence intensity in an aortic coarctation. *Ann. Biomed. Eng.* 40(4):860–870, 2012.

[2]Bazilevs, Y., M. C. Hsu, D. J. Benson, S. Sankaran, and A. L. Marsden. Computational fluid-structure interaction: methods and application to a total cavopulmonary connection. *Comput. Mech.* 77–89, 2009.

[3]Bazilevs, Y., M.-C. Hsu, Y. Zhang, W. Wang, X. Liang, T. Kvamsdal, R. Brekken, and J. Isaksen. A fully-coupled fluid-structure interaction simulation of cerebral aneurysms. *Comput. Mech.* 46:3–16, 2010. doi:10.1007/s00466-009-0421-4.

[4]Boussel, L., V. Rayz, A. Martin, G. Acevedo-Bolton, M. T. Lawton, R. Higashida, W. S. Smith, W. L. Young, and D. Saloner. Phase-contrast magnetic resonance imaging measurements in intracranial aneurysms in vivo of flow patterns, velocity fields, and wall shear stress: comparison with computational fluid dynamics. *Magn. Reson. Med.* 61(2):409–417, 2009.

[5]Brooks, A. N., and T. J. R. Hughes. Streamline Upwind/Petrov-Galerkin formulations for convection dominated flows with particular emphasis on the incompressible Navier-Stokes equations. *Comput. Methods Appl. Mech. Eng.* 1982.

[6]Cebral, J. R., M. A. Castro, J. E. Burgess, R. S. Pergolizzi, M. J. Sheridan, and C. M. Putman. Characterization of cerebral aneurysms for assessing risk of rupture by using patient-specific computational hemodynamics models. *Am. J. Neuroradiol.* 26:2550–2559, 2005.

[7]Chen, Y., D. J. J. Wang, and J. A. Detre. Testretest reliability of arterial spin labeling with common labeling strategies. *J. Mag. Reson. Imaging* 33(4):940–949, 2011.

[8]Colton, C. K., K. A. Smith, E. R. Merrill, and S. Friedman. Diffusion of urea in flowing blood. *AIChE J.* 17(4):800–808, 1971.

[9]Davies, N. P., and P. Jezzard. Selective arterial spin labeling (SASL): perfusion territory mapping of selected feeding arteries tagged using two-dimensional radiofrequency pulses. *Magn. Reson. Med.* 49(6):1133–1142, 2003.

[10]del Alamo, J. C., A. L. Marsden, and J. C. Lasheras. Recent advances in the application of computational mechanics to the diagnosis and treatment of cardiovascular disease. *Revista Espanola De Cardiologia* 781–805, 2009.

[11]Detre, J. A., J. S. Leigh, D. S. Williams, and A. P. Koretsky. Perfusion imaging. *Magn. Reson. Med.* 23(1): 37–45, 1992.

[12]Eastwood, J. D., C. A. Holder, P. A. Hudgins, and A. W. Song. Magnetic resonance imaging with lateralized arterial spin labeling. *Magn. Reson. Imaging* 20(8):583–586, 2002.

[13]Ford, M. D., N. Alperin, S. H. Lee, D. W. Holdsworth, and D. A. Steinman. Characterization of volumetric flow rate waveforms in the normal internal carotid and vertebral arteries. *Physiol. Meas.* 26(4):477–488, 2005.

[14]Gunther, M. Efficient visualization of vascular territories in the human brain by cycled arterial spin labeling MRI. *Magn. Reson. Med.* 56(3):671–675, 2006.

[15]Hendrikse, J., J. van der Grond, H. Lu, P. C. van Zijl, and X. Golay. Flow territory mapping of the cerebral arteries with regional perfusion MRI. *Stroke* 35(4):882–887, 2004.

[16]Jansen, K. E., C. H. Whiting, and G. M. Hulbert. A generalized method for integrating the filtered navierstokes equations with a stabilized finite element method. *Comput. Methods Appl. Mech. Eng.* 190(34):305–319, 2000.

[17]Kansagra, A. P., and E. C. Wong. Mapping of vertebral artery perfusion territories using arterial spin labeling MRI. *J. Magn. Reson. Imaging* 28(3):762–766, 2008.

[18]Kansagra, A. P., and E. C. Wong. Characterization of vascular territory changes following carotid artery compression using arterial spin labeling MRI. 2009.

[19]Krijger, J. K., B. Hillen, and H. W. Hoogstraten. Mathematical models of the flow in the basilar artery. *J. Biomech.* 22(11–12):1193–1202, 1989.

[20]Krijger, J. K., R. M. Heethaar, B. Hillen, H. W. Hoogstraten, and J. Ravensbergen. Computation of steady three-dimensional flow in a model of the basilar artery. *J. Biomech.* 25(12):1451–1465, 1992.

[21]Ku, J. P., M. T. Draney, F. R. Arko, W. A. Lee, F. P. Chan, N. J. Pelc, C. K. Zarins, and C. A. Taylor. In vivo validation of numerical prediction of blood flow in arterial bypass grafts. *Ann. Biomed. Eng.* 30(6):743–52, 2002.

[22]Ku, J. P., C. J. Elkins, and C. A. Taylor. Comparison of CFD and MRI flow and velocities in an in vitro large artery bypass graft model. *Ann. Biomed. Eng.* 33(3):257–269, 2005.

[23]Kung, E., A. Les, C. Figueroa, F. Medina, K. Arcaute, R. Wicker, M. McConnell, and C. Taylor. In vitro validation of finite element analysis of blood flow in deformable models. *Ann. Biomed. Eng.* 39:1947–1960, 2011. 10.1007/s10439-011-0284-7.

[24]Long C. C., M.-C. Hsu, Y. Bazilevs, J. A. Feinstein, and A. L. Marsden. Fluidstructure interaction simulations of the fontan procedure using variable wall properties. *Int. J. Numer. Methods Biomed. Eng.* 28(5):513–527, 2012.

[25]Lonyai, A., A. Dubin, J. Feinstein, C. Taylor, and S. Shadden. New insights into pacemaker lead-induced venous occlusion: simulation-based investigation of alterations in venous biomechanics. *Cardiovasc. Eng.* 84–90, 2010.

[26]Lutz, R. J., K. Warren, F. Balis, N. Patronas, and R. L. Dedrick. Mixing during intravertebral arterial infusions in an in vitro model. *J. Neurooncol.* 58(2):95–106, 2002.

[27]Marsden, A. L., M. Wang, J. E. Dennis, and P. Moin. Optimal aeroacoustic shape design using the surrogate management framework. *Optimiz. Eng.* 235–262, 2004.

[28]Marsden, A. L., A. J. Bernstein, R. L. Spilker, F. P. Chan, C. A. Taylor, and J. A. Feinstein. Large differences in efficiency among Fontan patients demonstrated in patient specific models of blood flow simulations. *Circulation* 480–480, 2007.

[29]Marsden, A. L., I. E. Vignon-Clementel, F. P. Chan, J. A. Feinstein, and C. A. Taylor. Effects of exercise and respiration on hemodynamic efficiency in CFD simulations of the total cavopulmonary connection. *Ann. Biomed. Eng.* 250–263, 2007.

[30]Marsden, A. L., M. Wang, J. E. Dennis, and P. Moin. Trailing-edge noise reduction using derivative-free optimization and large-eddy simulation. *J. Fluid Mech.* 13–36, 2007.

[31]Marsden, A. L., J. A. Feinstein, and C. A. Taylor. A computational framework for derivative-free optimization of cardiovascular geometries. *Comput. Methods Appl. Mech. Eng.* 1890–1905, 2008.

[32]Marsden, A. L., A. J. Bernstein, V. M. Reddy, S. C. Shadden, R. L. Spilker, F. P. Chan, C. A. Taylor, and J. A. Feinstein. Evaluation of a novel Y-shaped extracardiac fontan baffle using computational fluid dynamics. *J. Thorac. Cardiovasc. Surg.* 394–U187, 2009.

[33]Marsden, A. L., V. M. Reddy, S. C. Shadden, F. P. Chan, C. A. Taylor, and J. A. Feinstein. A new multiparameter approach to computational simulation for fontan assessment and redesign. *Congenit. Heart Dis.* 5(2):104–117, 2010.

[34]Mathew, G., L. Petzold, and S. Serban. Computational techniques for quantification and optimization of mixing in microfluidc devices. 2002.
[35]Mathew, G., I. Mezić, and L. Petzold. A multiscale measure for mixing. *Phys. D: Nonlinear Phenom.* 2005.
[36]Sankaran, S., C. Audet, and A. L. Marsden. A method for stochastic constrained optimization using derivative-free surrogate pattern search and collocation. *J. Comput. Phys.* 4664–4682, 2010.
[37]Sankaran, S., and A. L. Marsden. A stochastic collocation method for uncertainty quantification and propagation in cardiovascular simulations. *J. Biomech. Eng.* 133(3):031001, 2011.
[38]Schmidt, J. P., S. L. Delp, M. A. Sherman, C. A. Taylor, V. S. Pande, and R. B. Altman. The simbios national center: systems biology in motion. Proc. *IEEE Inst. Electr. Electron. Eng.* 96(8):1266, 2008.
[39]Shadden, S .C., and C.A. Taylor (2008) Characterization of coherent structures in the cardiovascular system. *Ann. Biomed. Eng.* 36(7):1152–1162.
[40]Shadden, S. C., F. Lekien, and J. E. Marsden. Definition and properties of lagrangian coherent structures from finite-time lyapunov exponents in two-dimensional aperiodicflows. *Phys. D: Nonlinear Phenom.* 212(34):271–304, 2005.
[41]Shadden, S. C., and V. C. Flow. (Version 1) [Computer Software]. http://mmae.iit.edu/shadden/software/, 2010.
[42]Spilt, A., F. M. A. Box, R. J. van der Geest, J. H. C. Reiber, P. Kunz, A. M. Kamper, G. J. Blauw, and Mark A. van Buchem. Reproducibility of total cerebral blood flow measurements using phase contrast magnetic resonance imaging. *J. Magn. Reson. Imaging* 16(1):1–5, 2002.
[43]Steinman D. A., J. S. Milner, C. J. Norley, S. P.Lownie, and D. W. Holdsworth. Image-based computational simulation of flow dynamics in a giant intracranial aneurysm. *Am. J. Neuroradiol.* 24:559–566, 2003. .
[44]Vignon-Clementel I. E., C. A. Figueroa, K. E. Jansen, and C. A. Taylor. Outflow boundary conditions for 3D simulations of non-periodic blood flow and pressure fields in deformable arteries. *Comput. Methods Biomech. Biomed. Eng.* 13(5):625–640, 2010.
[45]Wentland, A. L., O. Wieben, F. R. Korosec, and V. M. Haughton. Accuracy and reproducibility of phase-contrast mr imaging measurements for csf flow. *Am. J. Neuroradiol.* 31:1331–1336, 2010.
[46]Werner, R., K. Alfke, T. Schaeffter, A. Nabavi, H. M. Mehdorn, and O. Jansen. Brain perfusion territory imaging applying oblique-plane arterial spin labeling with a standard send/receive head coil. *Magn. Reson. Med.* 52(6): 1443–1447, 2004.
[47]Werner, R., D. G. Norris, K. Alfke, H. M. Mehdorn, and O. Jansen. Continuous artery-selective spin labeling (CASSL). *Magn. Reson. Med.* 53(5):1006–1012, 2005.
[48]Williams, D. S., J. A. Detre, J. S. Leigh, and A. P. Koretsky. Magnetic resonance imaging of perfusion using spin inversion of arterial water. *Proc. Natl Acad. Sci. USA.* 89(1):212–216, 1991.
[49]Wong, E. C. Vessel-encoded arterial spin-labeling using pseudocontinuous tagging. *Magn. Reson. Med.* 58(6):1086–1091, 2007.
[50]Yang, W. G., J. A. Feinstein, and A. L. Marsden. Constrained optimization of an idealized Y-shaped baffle for the Fontan surgery at rest and exercise. *Comput. Methods Appl. Mech. Eng.* 2135–2149, 2010.
[51]Yang, W., I. E. Vignon-Clementel, G. Troianowski, V. M. Reddy, J. A. Feinstein, and A. L. Marsden. Hepatic blood flow distribution and performance in conventional and novel Y-graft Fontan geometries: a case series computational fluid dynamics study. *J. Thorac. Cardiovasc. Surg.* 143(5):1086–1097, 2012.
[52]Zaharchuk, G., P. J. Ledden, K. K. Kwong, T. G. Reese, B. R. Rosen, and L. L. Wald. Multislice perfusion and perfusion territory imaging in humans with separate label and image coils. *Magn. Reson. Med.* 41(6):1093–1098, 1999.
[53]Zimine, I., E. T. Petersen, and X. Golay. Dual vessel arterial spin labeling scheme for regional perfusion imaging. *Magn. Reson. Med.* 56(5):1140–1144, 2006.